Selective Surface Reconstruction of a Defective Iridium-Based Catalyst for High-Efficiency Water Splitting

Yecan Pi[1], Leigang Li[1], Tu Sun[2], Lingzheng Bu[1], Yanhang Ma[2], Bolong Huang[3*], Zhiwei Hu[4], Chih-Wen Pao[5], Xiaoqing Huang[1,6*]

[1]College of Chemistry, Chemical Engineering and Materials Science, Soochow University, Jiangsu, 215123, China.

[2]School of Physical Science and Technology, Shanghai Tech University, Shanghai 201210, China.

[3]Department of Applied Biology and Chemical Technology, The Hong Kong Polytechnic University, Hung Hom, Kowloon, Hong Kong SAR.

[4]Max-Planck-Institute for Chemical Physics of Solids, Nöthnitzer Street 40, 01187, Dresden, Germany.

[5]*National Synchrotron Radiation Research Center, Hsinchu 30076, Taiwan.*

[6]*College of Chemistry and Chemical Engineering, Xiamen University, Xiamen 361005, China.*

*To whom correspondence should be addressed.

E-mail: bhuang@polyu.edu.hk, hxq006@suda.edu.cn

Abstract: As an essential demand for sustainable energy, achieving the electrocatalytic water splitting through highly efficient and low-cost catalysts still requires advanced synthetic strategies. Through the electrochemical reconstruction, the atomic-scale structural engineering has offered a promising platform to precisely tailor the electrocatalytic properties of nanomaterials. Herein, we reported an advanced electrocatalyst metal telluride ($IrTe_2$) with local disorder atomic

configuration for actualizing the highly efficient water reduction/oxidation electrocatalysis, which is precisely controlled by the electrochemical evolution. By the modulation of the flexible potential range in the electrochemical dealloying process of pristine $IrTe_2$ hollow nanoshuttles (HNSs), the reconstructed $IrTe_2$ HNSs with metallic Ir shell (D-$IrTe_2$) and oxidized IrO_x surface (DO-$IrTe_2$) are obtained at mild and high potential, respectively. For hydrogen evolution reaction, the D-$IrTe_2$ HNSs only requires an overpotential of only 54 mV to reach the current density of 10 mA cm^{-2} for in 1.0 M KOH, much lower than that of the state-of-the-art Pt (97 mV in 1.0 M KOH). Meanwhile, the DO-$IrTe_2$ HNSs displayed an outstanding turnover frequency (0.36 O_2 s^{-1} at 250 mV) for oxygen evolution reaction in 0.5 M H_2SO_4, surpassing most of the Ir-based catalysts. The local disorder atomic configuration in both D-$IrTe_2$ and DO-$IrTe_2$ HNSs are confirmed by the atomically resolved scanning transmission electron microscopy, displaying numerous structural defects and under-coordinated sites within the short-range ordered atomic arrangement. Operando X-ray absorption spectroscopic study identified the key role of the surface active layer under electrochemical condition for the distribution of microstrain, the reversible modification of electronic structure and the local environment. Density functional theory (DFT) calculations revealed that the tunable interfacial tellurization-alloying-oxidation endowed different local structural reconstructions and defects in modulating Ir-5*d* and O-2*p* bands to achieve mutual-self-activated multi-linear-scaling trends for both electronic and energetic evolution. The optimized electronic environment ultimately breakthroughs the barriers of sluggish full water splitting for pH-universal conditions with high interfacial current densities essentially maintained. This advanced structure reconstruction strategy opens the novel approach to achieve desired catalytic reactions, which is applicable to other material systems, and beyond.

The innovation of renewable energy economy is highly dependent on the development of efficient energy conversion and storage technologies[1-5]. One prospective way is to electrochemically convert natural molecules (e.g., water, carbon dioxide, and nitrogen) to value-added chemicals (e.g., hydrogen, hydrogen peroxide, alcohols, hydrocarbons and ammonia) driven by electricity from renewable energy sources[6-9]. Unfortunately, the sluggish kinetics of several key electrochemical reactions largely reduces the efficiency of those energy conversion devices. For example, as an attractive hydrogen production approach, the hydrogen evolution reaction (HER) kinetics in alkaline conditions is about orders of magnitude lower than that in acidic conditions, leading to poor efficiencies in alkaline electrolysers[10-12]. Oxygen evolution reaction (OER), an important anodic half reaction of providing protons and electrons for many energy conversion technologies, also severely suffers from sluggish kinetics. Even the state-of-the-art OER catalyst of Ir oxides requires considerable overpotential to achieve the desirable current density[13,14]. In particular, developing the bifunctional robust water-splitting electrocatalysts with exceptional activity toward both the HER and OER has always been the ultimate optimal solution for sustainable energy.

Over the past decades, substantial efforts have been devoted to the design and synthesis of highly active nanomaterials for various electrocatalytic applications. Benefiting from the collaborative theoretical and experimental efforts, a series of advanced nanomaterials with well-defined crystal facets and/or components have been developed, which have exhibited attractive catalytic activities for specific catalysis[15-18]. However, such structurally ordered nanomaterials usually undergo unprompted structural evolution under operating conditions, resulting in the obvious activity decay during electrocatalysis [19,20]. More importantly, the neglected structure evolution could also lead to a misunderstanding of the real structure-property relationship, for the reconstruction may be beneficial to the electrocatalytic performance in some cases. For example, some recent works have pointed out the occurrence of structural evolution of Pt-Ni catalysts during oxygen reduction reaction (ORR), where their outstanding activity may not be attributed to the initial alloy surface, but the formation of surface defectiveness structure by Ni leaching under catalytic conditions[21,22]. Similar results have also been reported for other alloys and perovskite electrocatalysts[23-27]. These unexpected structural evolutions of nanomaterials have challenged the traditional 'structurally ordered' catalyst design strategy. Meanwhile, designing 'structurally disordered' nanomaterials with various defects (e.g., vacancies, adatoms, boundaries, stacking faults, *etc*.) has shown promising opportunities for tailoring their properties, and been becoming a fresh strategy to achieve efficient catalysis[28-32]. Nonetheless, the prevalent approaches for introducing defects, including direct (synthetic control, doping, *etc.*) and indirect (calcination, ion exchange, etching, etc.) strategies, are usually complex and/or limited to specific material systems. Therefore, constructing defective nanomaterials via a facile and universal approach is still facing tremendous challenges[33-36]. Interestingly, the electrochemical reconstruction mentioned before may offer a new option to create robust defective structures, where the evolution of multicomponent nanomaterials under operating conditions is usually accompanied with component change and structure reconfiguration, thus may lead to the disordered atomic arrangement. Recently, the innovative multi-element strategy of combination between metal and semi-metal elements has attracted intense intention, which is beyond the conventional multi-metal alloys systems or metal-nonmetal systems. Nevertheless, facile and universal synthesis of homogeneous multi-component metal alloys or oxides still remains difficult as phase separation frequently occurs due to the vastly different properties of different components, which is unfavorable for the structure reconstruction. In this area, many of the disorder structures are simply achieved rather than well-controlled or understood. Additionally, structural evolution based on the preferential leaching (dealloying) of a non-noble metal component has limited the applicability of such strategy. More facile and general leaching is required to achieve universal and controllable structural evolution. More importantly, understanding the nature of the evolution process and revealing its connection with catalytic performance is crucial to broaden its applicability.

Most of the multi-elements electrocatalysts reported up to now have been generally confined to those consisting of transition metal alloys or the combination with unitary non-metal (S and P). The investigation of metal-like elements are very limited with great untapped potential. As a unique metal-like element, Te can form metal tellurides with most of the transition metals, and it can be easily leached under specific conditions, as revealed by the Pourbaix diagram, which makes the tellurides as appropriate candidates for facile and universal electrochemical reconstruction[37-38]. Inspired by the above knowledge, herein, using $IrTe_2$ as a model material, we present the fabrication of highly controllable local disorder atomic configuration through electrochemical reconstruction to achieve highly efficient water reduction/oxidation electrocatalysis. Specifically, the original $IrTe_2$ hollow nanoshuttles (HNSs) prepared by a facile one-pot hydrothermal method were reconstructed through controllable electrochemical leaching of Te (dealloying) in different potential ranges to form either metallic Ir shell (D-$IrTe_2$) at mild potentials or oxidized IrO_x surface (DO-$IrTe_2$) at high potentials. The newly constructed D-$IrTe_2$ HNSs exhibit high HER turnover frequency in alkaline conditions (0.71 H_2 s^{-1} at 20 mV of overpotential in 1.0 M KOH), much higher than that of Pt/C (0.14 H_2 s^{-1}). The small Tafel slope (49.4 mV dec^{-1}) and high turnover frequency (0.36 O_2 s^{-1} at 250 mV of overpotential) of DO-$IrTe_2$ HNSs in 0.5 M H_2SO_4 make it among the most active acidic OER catalysts. By coupling the D-$IrTe_2$ and DO-$IrTe_2$ into a water splitting electrolyzer, the D-$IrTe_2$ || DO-$IrTe_2$ delivers remarkable activity for overall water splitting with much lower cell voltage than that of Pt/C || IrO_2 in both 1.0 M KOH and 0.5 M H_2SO_4.

The combined aberration-corrected scanning transmission electron microscopy (STEM), operando X-ray absorption spectroscopy (XAS) analysis reveals the generation of local disorder atomic configuration in both D-$IrTe_2$ HNSs and DO-$IrTe_2$ HNSs during the electrochemical reconstruction, which features widely distributed structural defects, under-coordinated sites and microstrain, and promoting the flexible electronic and local structure. Density functional theory (DFT) calculations confirm the self-generated reconstructions of defective interfaces induced by the tellurization-alloying-oxidation are serving as active sites with various oxidation states to actualize a variety of mutual-activated p-d inter-orbital electron transfers. The interface unsaturated lattice-O sites exhibit the optimal *p-d* electron transfer with Ir-e_g-t_{2g} gap crossover, which guarantees the substantial competitively preferred H-O-H scissoring in both alkaline HER and OER catalysis. Our work shows that the formation of local disorder atomic configuration during electrochemical reconstruction plays an indispensable role in achieving the superior electrocatalytic performance of $IrTe_2$ HNSs, which provides a new avenue for the fabrication of efficient electrocatalysts.

Results and discussion

Fabrication of D-$IrTe_2$ and DO-$IrTe_2$ HNSs from pristine $IrTe_2$ HNSs. Pristine $IrTe_2$ HNSs were prepared by reducing iridium (III) acetylacetonate and potassium tellurite in a mixture of ethylene glycol and water (see Methods for details). Transmission electron microscopy (TEM) and high-angle annular dark-field scanning TEM (HAADF-STEM) images (**Supplementary Fig. 1**) show the hollow and shuttle-like morphology of the $IrTe_2$ HNSs. The length and diameter were determined to be 104.6 ± 9.6 nm and 37.6 ± 4.5 nm, respectively. After being supported on carbon, the $IrTe_2$ HNSs were annealed at 250 ºC for 1 h (**Supplementary Fig. 2**).

To tailor the surface structure of pristine $IrTe_2$ HNSs through electrochemical reconstruction, we performed controllable electrochemical dealloying and surface oxidation to generate the D-$IrTe_2$ and DO-$IrTe_2$ HNSs, respectively, on the basis of the Pourbaix diagrams (see Methods for details). A schematic diagram illustrating the electrochemical transformation strategy is shown in **Fig. 1a**. As one of the proposals, pristine $IrTe_2$ HNSs were dealloyed at a mild potential range. With lower stability than Ir, Te was selectively etched during the electrochemical process, resulting in the formation of metallic Ir shell in the D-$IrTe_2$ HNSs. The evolution could be evidenced by the cyclic voltammogram curves, in which the redox peaks of Te disappeared gradually, and hydrogen adsorption charge increased simultaneously and finally reached its maximum value during the potential cycling (**Supplementary Fig. 3a**). Alternatively, under higher operating potentials, electrochemical Te leaching and Ir oxidation have occurred simultaneously, leading to IrO_x surface in the DO-$IrTe_2$ HNSs. The tiny hydrogen adsorption charge of DO-$IrTe_2$ HNSs also implies the oxidation state of surface Ir (**Supplementary Fig. 3b**).

To further clarify the morphology and composition evolutions of $IrTe_2$ HNSs, TEM, HAADF-STEM and energy-dispersive X-ray spectroscopy (EDS) analysis for the pristine $IrTe_2$, D-$IrTe_2$ and DO-$IrTe_2$ HNSs were performed. As shown in **Fig. 1b&d&f** and **Supplementary Fig. 4**, the profile of HNSs has been largely maintained after the electrochemical reconstruction, while the highly porous feature can be clearly observed for both D-$IrTe_2$ and DO-$IrTe_2$ HNSs. Besides, the Ir/Te ratios were determined to be 53.1/46.9 and 87.8/12.2 for D-$IrTe_2$ and DO-$IrTe_2$ HNSs, respectively, confirming the distinct Te loss (**Supplementary Fig. 5**). EDS line scan analysis and element mapping was employed to further evidence the component distributions of different HNSs. As revealed in **Fig. 1c** and **Supplementary Fig. 6a**, the uniform distribution of Ir and Te at pristine $IrTe_2$ HNS is consistent with their metal telluride characteristic. After a mild electrochemical dealloying process, although a certain amount of Te remained in the D-$IrTe_2$ HNSs, the relative intensity of Ir and Te implies a clear Ir enrichment in the surface, as confirmed by the line scan analysis (**Fig. 1e** and **Supplementary Fig. 6b)**. Regarding the DO-$IrTe_2$ HNSs, a serious loss of Te can be deduced from the significantly reduced signal (**Fig. 1g** and **Supplementary Fig. 6c)**. It is conceivable that the dealloying process was promoted by increased operating potential. The surface composition and chemical state evolution of $IrTe_2$ HNSs were further analyzed by X-ray photoelectron spectroscopy (XPS) (**Supplementary Fig. 7**). The Ir 4f regions for $IrTe_2$ and D-$IrTe_2$ HNSs show similar binding energy corresponding to metallic Ir, which can be attributed to the similar electronegativity of Ir (χP: 2.20) and Te (χP: 2.10). The Te 3d signal of D-$IrTe_2$ HNSs decreases considerably compared to the pristine $IrTe_2$ HNSs, consistent well with the formation of metallic Ir shell. For the DO-$IrTe_2$ HNSs, there is a double of new peaks at higher binding energy, indicating the partial oxidation of surface Ir, which is further verified by the Raman spectra (**Supplementary Fig. 8**). Moreover, the negligible Te 3d signal of DO-$IrTe_2$ HNSs further reveals the serious leaching of surface Te. Therefore, via controlled electrochemical evolution strategy, we have successfully created two distinct catalysts with either metallic Ir shell or IrO_x surface from the pristine $IrTe_2$ HNSs.

Electrochemical evaluation. To investigate the electrochemical performance of D-$IrTe_2$ and DO-$IrTe_2$ HNSs, we carried out HER/OER measurements with a standard three-electrode system. It is well-known that the kinetics of HER in basic environment is relatively sluggish, and even the activity of the state-of-the-art Pt is approximately two orders of magnitude lower than that in acidic media. We first investigated the HER performance of D-$IrTe_2$ with metallic Ir shell in basic electrolytes. For comparison, commercial Ir (Premetek, 20 wt.% Ir on Vulcan carbon black, referred to Ir/C) and Pt (Johnson Matthey, 20 wt.% Pt on Vulcan carbon black, referred to Pt/C) were also measured under the same conditions. **Fig. 2a** shows the polarization curves of various catalysts acquired in 1.0 M KOH, and the current is normalized to the geometric area of electrode. Remarkably, the D-$IrTe_2$ HNSs showed a very small overpotential of 54 mV at the current density of 10 mA cm^{-2}, much lower than that of the state-of-the-art Pt/C (97 mV) and Ir/C (137 mV), suggesting the superior HER activity of D-$IrTe_2$ HNSs in basic electrolyte. The Tafel slope of D-$IrTe_2$ HNSs was 32.6 mV dec^{-1}, which is 7.1 and 13.5 mV dec^{-1} lower than that of Pt/C and Ir/C, respectively (**Fig. 2b**). Moreover, by extrapolating the Tafel plot, the exchange current density of D-$IrTe_2$ HNSs is calculated to be 0.405 mA cm^{-2}, which is around 2.5 times higher than that of Pt/C (0.161 mA cm^{-2}), indicating their superior reaction kinetics in alkaline solution[12]. For more comprehensive electrochemical activity evaluation, the current densities were normalized to the mass (J_{mass}) and electrochemical surface area ($J_{specific}$) of the catalyst (**Supplementary Fig. 9**). As shown in **Fig. 2c**, the D-$IrTe_2$ HNSs exhibited 3.1 times higher of J_{mass} and 5.8 times higher of $J_{specific}$ than that of Pt/C at the same potential of -0.05 V vs. RHE, revealing the superior activity of D-$IrTe_2$ HNSs over Pt/C in alkaline solution. Furthermore, electrochemical impedance spectroscopy (EIS) measurements were conducted to investigate the charge-transfer resistance (R_{ct}), an important parameter to evaluate the intrinsic kinetic property of electrocatalyst. **Fig. 2d** shows the Nyquist plots of D-$IrTe_2$ HNSs, Pt/C and Ir/C, and the fitted R_{ct} values are 27.1, 54.5 and 91.2 Ω, respectively. The smallest R_{ct} value of D-$IrTe_2$ HNSs suggests the fastest interfacial charge transfer kinetics for HER catalysis. Turnover frequency (TOF) is another convincing parameter that is widely used to evaluate the intrinsic activity of catalysts. Inspiringly, the D-$IrTe_2$ HNSs exhibit a very high TOF value at a small overpotential (1.18 H_2 s^{-1} at 25 mV), which is over 6.2 times greater than that of Pt/C (0.19 H_2 s^{-1} at 25 mV) and also much larger than that of other well-developed HER catalysts (**Fig. 2e**). The ultra-high TOF value of D-$IrTe_2$ HNSs further indicates its excellent catalytic activity for HER in alkaline conditions. Electrochemical stability of D-$IrTe_2$ HNSs was also evaluated using a chronopotentiometry test. As shown in **Fig. 2f**, the D-$IrTe_2$ HNSs displayed minor potential fluctuation after long-term electrolysis at a current density of 10 mA cm^{-2}, which is much better than that of Pt/C. In addition, the HER activities in less alkaline condition (0.1 M KOH) and acidic conditions (0.5 M and 0.05 M H_2SO_4) were also investigated. In 0.1 M KOH solution, the D-$IrTe_2$ HNSs exhibited higher current density, lower Tafel slope and charge-transfer resistance compared to that of both Ir/C and Pt/C (**Supplementary Figs 10-11**). Detailed comparisom with the reported HER electrocatalysts are summarized in

Supplementary **Table S1**. Regarding the HER activity in acidic solutions, the D-$IrTe_2$ HNSs also displayed excellent activity comparable to that of Pt/C (**Supplementary Fig. 12**). These results make D-$IrTe_2$ HNSs among the most active HER electrocatalysts in both alkaline and acid conditions. Meanwhile, we also evaluated the HER performance of DO-$IrTe_2$ HNSs, which exhibited the minimal current in the measured potential range, most likely due to the weak HER activity of oxidized Ir surface (**Supplementary Fig. 13**).

OER is another important half reaction for many energy conversion technologies, but its slow kinetics has limited the performance and commercialization of such devices[39-41]. To date, iridium oxide is the most appropriate OER catalyst, especially in acidic media, but the development of more efficient and low-cost Ir-based catalysts still remains difficult[42-46]. Therefore, we exclusively evaluated the electrocatalytic properties of DO-$IrTe_2$ HNSs with the electrochemically oxidized Ir surface toward OER, and the commercial IrO_2 (Alfa Aesar) and electrochemical oxidized Ir/C (referred to O-Ir/C) were measured under the same conditions for comparison. **Fig. 3a** shows the OER polarization curves of various catalysts in 0.5 M H_2SO_4. DO-$IrTe_2$ HNSs exhibited the highest OER activity requiring an overpotential of 298 mV to reach the current density of 10 mA cm^{-2}, much lower than that of O-Ir/C (323 mV) and IrO_2 (334 mV). In addition, the Tafel slope of DO-$IrTe_2$ HNSs was measured to be 49.4 mV dec^{-1}, which is smaller than that of O-Ir/C (58.4 mV dec^{-1}) and IrO_2 (56.0 mV dec^{-1}), indicating the fastest OER kinetics of DO-$IrTe_2$ HNSs (**Fig. 3b**). For cost considerations, the iridium-mass-based activities of different catalysts were also compared. As shown in **Fig. 3c**, the DO-$IrTe_2$ HNSs can deliver a current density of 213.8 A g_{Ir}^{-1} at the overpotential of 300 mV, revealing 2.3 and 3.2 times improvement compared to the O-Ir/C (92.3 A g_{Ir}^{-1}) and IrO_2 (66.1 A g_{Ir}^{-1}), respectively. To elucidate the intrinsic activity of accessible Ir sites, the OER current normalized to the number of electrochemically accessible iridium sites (determined by the anodic redox peak of Ir, **Supplementary Fig. 14**) was compared. As can be seen in **Fig. 3c**, DO-$IrTe_2$ HNSs showed more than 3.4 times higher specific OER activity than that of IrO_2 at 1.5 V vs. RHE. The electrochemical stability of DO-$IrTe_2$ HNSs was also manifested by a prolonged chronopotentiometry test (**Supplementary Fig. 15**). To ensure that the observed anodic current was from oxidation of water instead of the catalyst components (e.g., Ir or Te), rotating ring-disk electrode (RRDE) measurement was performed (**Fig. 3d**, **Supplementary Fig. 16**)[16,47]. The OER Faradaic efficiency of DO-$IrTe_2$ HNSs was calculated to be ~100%, proving that the oxidation current originates exclusively from water oxidation. Moreover, the OER activity evaluation in 0.05 M H_2SO_4 was also performed. Compared to IrO_2 and O-Ir/C, the DO-$IrTe_2$ HNSs showed obvious advantages in terms of overpotential and Tafel slope, as well as mass and specific activities (**Supplementary Figs 17-18**). In order to further assess the intrinsic OER activity, the TOF of DO-$IrTe_2$ HNSs was estimated and compared with that of reported OER electrocatalysts in acidic condition (**Fig. 3e**). As can be seen, the DO-$IrTe_2$ HNSs give outstanding TOF values in 0.5 M H_2SO_4 (0.36 O_2 s^{-1} at 250 mV; 1.55 O_2 s^{-1} at 280 mV), surpassing many reported Ir- and Ru-based catalysts, making it among the most efficient OER catalysts in acidic condition. Meanwhile, the OER performance of D-$IrTe_2$ HNSs was also studied, which demonstrated the comparable activity to that of the DO-$IrTe_2$ HNSs (**Supplementary Figs 19**). It is worth emphasizing that a large oxidation current appeared during the initial polarization process of D-$IrTe_2$ HNSs in the OER potential region, implying the oxidation of surface metallic Ir. The OER performance of DO-$IrTe_2$ HNSs was further investigated in alkaline conditions (i.e., 0.1 M and 1.0 M KOH), which also exhibits superior activities compared to that of O-Ir/C and IrO_2 (**Fig. 3f** and **Supplementary Figs 20-21**). Detailed comparisom with the reported OER electrocatalysts are summarized in Supplementary **Table S2**. These results indicate the potential of DO-$IrTe_2$ HNSs as an efficient and pH-universal catalyst for OER.

Encouraged by the excellent HER performance of D-$IrTe_2$ and OER performance of DO-$IrTe_2$ at broad pH range, we performed overall water splitting catalysis by coupling D-$IrTe_2$ and DO-$IrTe_2$ as the cathode and anode catalyst, respectively, in both 0.5 M H_2SO_4 and 1.0 M KOH. As indicated by the polarization curves (**Supplementary Fig. 22**), the D-$IrTe_2$ || DO-$IrTe_2$ can achieve a current density of 11.8 mA cm^{-2} in 0.5 M H_2SO_4 and 17.9 mA cm^{-2} in 1.0 M KOH at the cell voltage of 1.6 V, which is approximately 2.34 and 3.86 times higher than that of commercial Pt/C || IrO_2, respectively, implying their great potential for pH-universal overall water splitting.

Local disorder atomic configuration of D-$IrTe_2$ and DO-$IrTe_2$ HNSs. To gain insight into the mechanism for the superior electrocatalytic activities of D-$IrTe_2$ and DO-$IrTe_2$ HNSs, atomic-scale STEM/EDS analysis were performed to characterize the morphology, electronic structure and local structure. **Fig. 4a** shows the high-resolution HAADF-STEM image and the corresponding fast Fourier transform (FFT) image of a D-$IrTe_2$ HNS. Obviously, there are plenty of pits and pores over the whole HNS, which is proved to be polycrystalline. High-resolution elemental mappings show a clear Ir shell of approximately 5 nm in D-$IrTe_2$ HNS (**Fig. 4b**). The highly porous feature was also observed in the DO-$IrTe_2$ HNSs, where the larger pores indicate a higher degree of Te leaching (**Supplementary Fig. 23**). Considering that the substantial leaching of Te will destroy the original structure of metal telluride and lead to an atomic rearrangement, numerous structural defects may be generated in the D-$IrTe_2$ HNSs and DO-$IrTe_2$ HNSs (**Fig. 4c**). To prove this conjecture, atomic-resolution HAADF-HRSTEM was employed to investigate the atomic arrangement in D-$IrTe_2$ HNSs and DO-$IrTe_2$ HNSs. As shown in **Figs. 4d-f**, the crystalline area is interrupted by irregular holes, resulting in abundant of under-coordinated surface sites at steps and corners in the D-$IrTe_2$ HNSs. Substantial twins, grain boundaries, as well as stacking faults can also be found over the HNS, indicating their highly defective structure. Furthermore, there are plenty of ordered regions between these disordered regions with precise atomic arrangement within the D-$IrTe_2$ HNSs, which can be corresponded to the face-centered cubic (*fcc*) Ir

(**Fig. 4g**). Similar phenomenon can also be observed in the DO-$IrTe_2$ HNSs (**Figs. 4h-i**, **Supplementary Fig. 23b**).

To gain more in-depth insight into the detailed electronic structure and nature of such unique local disorder atomic arrangement, X-ray absorption near edge structure (XANES) spectroscopy and extended X-ray absorption fine structure (EXAFS) spectroscopy were performed (**Supplementary Fig. 24**, see Methods for more details of XAS measurements). Firstly, the oxidation state of Ir in of D-$IrTe_2$ HNSs and DO-$IrTe_2$ HNSs under the electrochemical reaction was determined using the Ir L_3-edge XANES spectra, which is well known to be very sensitive to the oxidation state of Ir[48]. In general, XANES and EXAFS spectra obtained in transmission mode are bulk-sensitive techniques, however XAS spectra on our materials with very thin shell of unique hollow structure of the D-$IrTe_2$ HNSs and DO-$IrTe_2$ HNSs can provides the information of electronic structure and local environment mainly from surface active layers (**Supplementary Fig. 25**). As shown in **Fig. 5a**, the Ir-L_3 XANES spectrum of D-$IrTe_2$ has a same energy position of white line as that of the pristine $IrTe_2$ and Ir/C, indicating the same oxidation state of Ir ions, namely the same chemical redox state in consistence with the result from above XPS. In contrast, the white line position of DO-$IrTe_2$ HNSs shows a slightly higher shift by 0.3 eV relative to that of D-$IrTe_2$ HNSs revealing the increased d-band hole due to the electrochemical oxidation, yet it is still lower than that of IrO_2 ($5d^5 6s^0$). *In-situ* XANES measurements were conducted to investigate the evolution of the electronic structure during electrocatalysis. As shown in **Figs. 5b-c**, when the applied potential is decreased from 0.1 V_{RHE} to -0.024 V_{RHE}, no obvious change in the Ir-L_3 XANES spectra is noticed for D-$IrTe_2$ HNSs and Ir/C. This means that the electronic structure remains unchanged during HER. In sharp contrast, the Ir-L_3 XANES spectra are shifted to higher energies by +0.3 eV for DO-$IrTe_2$ HNSs (see the top of **Fig. 5d**), and 0.6 eV for IrO_2 (see the top of **Fig. 5e**) upon applied potential going from 0.5 V_{RHE} to 1.51 V_{RHE}, indicating an increase of the hole in the Ir 5*d* orbitals during OER process

(**Figs. 5d-e**). Moreover, as the applied potential returns to 0.5 V_{RHE}, the spectrum of DO-IrTe$_2$ HNSs is shifted back to its initial state (dotted line in **Fig. 5d**), while the spectrum of IrO$_2$ still remains at the energy position under high potential (dotted line in **Fig. 5e**). We conclude that DO-IrTe$_2$ HNSs and IrO$_2$ have a reversible and irreversible oxidation state transition, respectively. Simultaneously, the local ligand environment around Ir sites in D-IrTe$_2$ and DO-IrTe$_2$ HNSs were investigated by EXAFS analysis and compared with that of Ir/C, bulk IrTe$_2$ and rutile IrO$_2$. As shown in **Fig. 5f**, the simulations of Fourier transforms of EXAFS spectra revealed the presence of Ir-Ir bond in the D-IrTe$_2$ HNSs, confirming the metallic Ir shell structure of D-IrTe$_2$ HNSs. In case of DO-IrTe$_2$ HNSs, an additional feature related to the Ir-O bond apparently appears, which is consistent with their oxidized Ir surface (**Fig. 5g**). Furthermore, to track the instantaneous local structure of the catalysts under electrocatalytic conditions, the evolution of Ir-Ir and Ir-O bond length in D-IrTe$_2$ and DO-IrTe$_2$ HNSs under the applied electrode potential was investigated. As shown in **Supplementary Fig. 26**, the Ir-Ir distances in both D-IrTe$_2$ HNSs and Ir/C show no noticeable change when the applied potential was stepped to HER region, while the Ir-Ir distance in the former (2.692 Å) was shorter than that of Ir/C (2.708 Å) and Ir foil (2.712 Å) suggesting a compressive stress. (**Supplementary Table 3**). On the contrary, the Ir-O distance in IrO$_2$ decreased from 2.027 Å to 1.989 Å when the applied potential increased from 0.5 to 1.51 V_{RHE}, and maintained at this value when the applied potential was switched back to 0.5 V_{RHE} (**Fig. 5h**). Similarly, the Ir-O distance in DO-IrTe$_2$ HNSs also decreased from 2.051 Å to 2.028 Å with increasing potential, whereas the average bond length for Ir-O in DO-IrTe$_2$ HNSs was longer than that of IrO$_2$. It is interesting to note that this evolution is reversible for DO-IrTe$_2$ HNSs, as the Ir-O bond returns back to its original length after the potential was switched back to 0.5 V_{RHE} (**Fig. 5i**, **Supplementary Table 3**). Generally, the transition metal-oxygen bond length decreases with increasing valence state of the metal ion due to the reduced effective ionic radius[49]. The shortening of the Ir-O bonds in DO-IrTe$_2$ HNSs and

IrO_2 reveals the transition of Ir species to higher oxidation states during OER. This indicates again a reversible evolution of oxidation state of Ir ion in DO-$IrTe_2$ HNSs in agreement with the results of XANES observed above. The DO-$IrTe_2$ HNSs displays longer average Ir-O distance was close to the reported value for hydroxo species (Ir^{3+}-OH)[50]. The O 1s XPS spectra also revealed the presence of the hydroxide surface species (OH: O ratios of 0.49 and 0.10 for DO-$IrTe_2$ HNSs and IrO_2, respectively) (**Supplementary Fig. 27**). Considering all results observed above, we propose the formation of iridium hydroxide surface species (IrO_xH_y) with a mixed Ir oxidation state ($Ir^{3+}$and Ir^{4+}) on the surface of DO-$IrTe_2$ HNSs, which results in a longer average Ir-O distance and the reversible oxidation-reduction cycles during OER.

All above experimental observations demonstrate the formation of local disorder atomic configuration during controllable electrochemical evolution revealing unique flexible electronic and local structure. We speculate that the leaching of Te breaks the long-range order and leads to atomic rearrangement, in turn produces a large number of lattice defects and under-coordinated sites at steps and corners, as clearly revealed by the atomic-resolution HAADF-HRSTEM images. Introducing defects could generate widely distributed lattice microstrain, where the Ir-Ir bond in D-$IrTe_2$ HNSs is ~0.4 to 0.7% shorter than that of bulk Ir metal (Ir foil) as revealed by EXAFS analysis. As compared with an ordered flat surface, the under-coordinated atoms at defects, steps and kinks tend to show characteristic chemisorption to various ligands ranging from oxo (O), hydroxo (OH) to aqua (OH_2)[51]. As discussed above, the DO-$IrTe_2$ HNSs exhibits longer average Ir-O bond compared to IrO_2, which can be explained by their characteristic difference in the surface iridium species (IrO_xH_y). Additionally, different from the previously reported hydroxo species that were usually dominant at low electrode potential, DO-$IrTe_2$ HNSs possessed relatively high hydroxide content at the OER potential region, as revealed by their longer Ir-O bond, which could be attributed to the stabilization of Ir-OH species at defects and under-coordinated sites of the local disorder atomic configuration giving rise to optimized intermediate adsorption and reaction path, and thus boosting the electrocatalysis[52,53]. Furthermore, the relatively loose atomic connection in disordered regions makes the local disordered configuration more flexible compared to that of the ordered structure with periodically linked atoms, and also, differ from the completely unconstrained atomic arrangement of amorphous structures, acting like a spring that can flexibly switch back and forth within a certain range. This metaphor can be confirmed by operando XAS experiments as discussed above, where the DO-$IrTe_2$ HNSs shows reversible redox behavior and local structure evolution during OER. Considering that OER involves complex multi-electron transfer steps, more flexible electronic and local structure may be beneficial to adsorption and dissociation of different intermediates, and thus promote the reaction.

DFT simulations of local disordered configurations. DFT simulations were performed to get further insight to the exceptional catalytic performance of D-$IrTe_2$ and DO-$IrTe_2$ HNSs, and both as-built $Ir||IrTe_2$ and $IrO_2||IrTe_2$ models have considered the experimentally observed structural defective features including nanopores, voids, troughs and convex-concave surface distortions, etc. These defective regions contain enormous edge atoms and step-sites with under-coordinated Ir- and O- sites, which inevitably induce local short-range disorder (SRDO) with lattice strains. Consequently, the self-activated reconstruction induced the corresponding electronic structures of the various local systems are evidently modified, confirmed by the real spatial bonding and anti-bonding orbitals near the Fermi level (E_F). In particular, surface cracking areas with the trough reconstructed within the $IrO_2||Ir||IrTe_2$ interface demonstrates the most electron-rich character, supporting the high electroactivity near the atomic defective regions (**Fig. 6a**). The electronic structure of under-coordinated O-sites within the interfacial trough reconstruction region between IrO_2 and Ir parts reveals that especially to the CN=1, mostly displays high electronic activities with the O-2*p* band crossover the E_F, which crucially contributes high interface current densities as well as the electron-transfer between surface and intermediate adsorbates. Consistently, the PDOSs of O-2*p* band variation trend supports the gradual activation of the inter p-orbital electron-transfer from the ordered bulk lattice towards the SRDO interface region (**Fig. 6b**). On the contrary, the Ir-5*d* band from the Ir||$IrTe_2$ interface shows the smoothly downward from the bulk $IrTe_2$ towards surface Ir-sites. The 5*d*-band center shifts from E_V-1.7 eV to E_V-3.5 eV. Both the t_{2g} and e_g components of Ir-5*d* band overall move downward to alleviate the Ir-H over-binding effect with electron-transfer efficiency remained (**Fig. 6c**). Consistent with the experimental XAS characterization, the local SRDO lattice of IrO_2 layer displays relatively loosen and flexible atomic bonding, endowing under-coordinated edge atoms paved for a variety of as-observed reconstructions. Especially to the Ir surface atoms or step-site, their 5*d* orbitals substantially un-saturated for p-d orbital overlapping elevates the electron-transfer rate levels for both interfacial and surface-to-adsorbates at the largest current density extent. From the bulk IrO_2 layer towards the atomically reconstructed interfacial region, the Ir-5*d* bands continuously broaden with the gap between t_{2g} and e_g narrowed at the meanwhile. This trend increases the probabilities of on-site p-d overlapping for higher electron-transfer efficiency between Ir and O-species (**Fig. 6d**). Accordingly, we compared the overall Ir-5*d* band contribution among $IrTe_2$, Ir, and IrO_2 systems, in which the Ir-5*d* bands present the dominant character near the E_F. However, with appropriate Ir and IrO_2 reconstructed layer modification, the electronic activities of Ir-5*d* band are further activated with wider range (**Fig. 6e**). We further found the E_V-3.8 eV to E_V-7.9 eV are the p-orbital range of H_2O and adsorbing *OH for optimal overlapping with Ir-5*d* band of surface Ir-sites from Ir||$IrTe_2$ interfacial reconstructed system. This feature combining with Ir-5*d* band character crucially ensures the superior HER performance within both acidic and alkaline conditions (**Fig. 6f**).

The detailed site-dependent PDOSs of the O-2*p* bands indicate the high electronic activities of the reconstructed defective IrO_2 regions, especially to the surface dangling O-sits with one-fold coordinated.

On the counterpart, we also laid out the p-bands of various O-species which sequentially occurred from the four-electron process. The free H_2O must experience an electron-injection step to activate the non-bonding O-2*p* lone-pair p-π electron for energetically favored adsorption. From the levels of lower p-σ components that bonding with H, there are two linear-scaled p-orbital leverage effects shifting up towards p-π long pair states of adsorbing O=O. This indicates the energetic pathway linear-scaled trend is not sufficient to support superior OER catalysis. Meanwhile, the satisfaction of the electronic orbital linear-scaled physicochemical trend is also essential to guarantee the barrier-free electron-transfer of H_2O oxidation (**Fig. 6g**). The mechanical correlation based on the Lame parameter shows that the larger for the modulus, the higher stabilities of interface binding after reconstruction. However, the *Volcano-Plot* exhibits the correlation that the higher strain potentially increases the barrier of surface electron-transfer towards the O-species, proving the experimental characterizations (**Fig. 6h**).

To identify the role of different reconstructed interfacial region in water-splitting electrocatalysis, the HER and OER performance from energetic perspectives have also been unveiled. The H-adsorption is energetically favorable while the H_2 level prefers the desorption (**Fig. 6i**). Further adsorption energy comparison between Ir||$IrTe_2$ and IrO_2||Ir||$IrTe_2$ shows the optimal HER proceeds within the Ir||$IrTe_2$ interface region, supporting the experimental results (**Fig. 6j**). Typically, the alkaline HER catalysis suffers the low kinetic rate, which is heavily limited at the initial H-O cleavage of H_2O splitting. Both Ir||$IrTe_2$ and IrO_2||Ir||$IrTe_2$ interface systems demonstrate the prominent alkaline HER performance, while the IrO_2||Ir||$IrTe_2$ slightly outperformed the Ir||$IrTe_2$ based on the superior H_2O splitting capability (**Fig. 6k**) with a lower uphill barrier in the transition state for H_2O-splitting in IrO_2||Ir||$IrTe_2$ (**Fig. 6l**). For OER performance, both alkaline and acidic OER pathways are energetically favorable under U=0 V, with the same potential determining step occurred at the formation of [$*OOH^-$]. This character originates from the prominent electron-transfer behavior of under-coordinated lattice-O sites within the mutual-self-activated defective interface region, which effectively coupling the O-2p-π lone-pair non-bonding orbitals of H_2O towards efficient H_2O splitting process (**Fig. 6m**). At the potential of U=1.23 V, the evident difference has been exhibited. The acidic pathway possesses lower overpotential height for overcoming the barrier of forming [*OOH^-]. Therefore, the interface system IrO_2||Ir||$IrTe_2$ presents higher performance in acidic OER catalysis (**Fig. 6n**). Through detailed theoretical explorations, we confirm that the essential rate determining step/potential determination step for both HER and OER occurs within the same step of initial O-H bond cleavage, where the reconstructed IrO_2||Ir||$IrTe_2$ interface with abundant short-range disorder reaches this criterial. Overall, the local self-reconstructed interfacial region optimizes both the electroactivity of Ir||$IrTe_2$ and IrO_2||Ir||$IrTe_2$, which synergistically contributes substantially to competitive full water splitting performance for efficient HER and OER.

Conclusion

In conclusion, we have fabricated two distinct Ir-based electrocatalysts through precise electrochemical reconstruction of $IrTe_2$ HNSs, which are highly efficient for HER and OER catalysis. Specifically, pristine $IrTe_2$ HNSs is converted to D-$IrTe_2$ HNSs with metallic Ir shell *via* an electrochemical dealloying process at a mild potential range. The D-$IrTe_2$ HNSs displays remarkable HER activity under both alkaline and acidic conditions, with a TOF of 0.71 H_2 s^{-1} at -0.02 V vs. RHE in 1.0 M KOH solution, over 5 times higher than that of the commercial Pt/C (0.14 H_2 s^{-1}). On the other hand, the DO-$IrTe_2$ HNSs prepared through electrochemical dealloying accompanied with oxidation of pristine $IrTe_2$ HNSs at higher potentials features an oxidized Ir surface, which shows appealing OER performance in universal pH media, surpassing most of the reported well-developed Ir- and Ru-based catalysts. Further atomically resolved STEM and operando XAS characterizations identified the local disorder atomic configuration in D-$IrTe_2$ HNSs and DO-$IrTe_2$ HNSs, which possess wide distribution of structural defects and under-coordinated sites, and promote the flexible electronic and local structure.

DFT calculations further reveal that the competitively preferred H-O-H scissoring dominated HER and OER performance with substantially desirable current density originates from the short-range disordered (SRDO) interfacial reconstruction region. With precisely engineered interfacial tellurization-alloying-oxidation, active SRDO self-reconstructed regions with abundant under-coordinated lattice-O sites superiorly promote electron-transfer and achieve multi-linear-scaling trends for both electronic and energetic evolutions. Thus, the D-$IrTe_2$ HNSs and DO-$IrTe_2$ HNSs essentially maintain a high interfacial current density to ultimately breakthrough barrier of sluggish full water splitting within pH-universal conditions. This work proposed a facile and universal strategy for the construction of advanced catalysts with local disorder atomic configuration via precise electrochemical reconstruction. In a broader context, our present study provides a new inspiration for the development of heterogeneous catalysts.

Materials and methods

Chemicals. Iridium (III) acetylacetonate ($C_{15}H_{21}IrO_6$, $Ir(acac)_3$) was purchased from Tokyo Chemical Industry Co., Ltd. Potassium tellurite (K_2TeO_3, 97%), ascorbic acid ($C_6H_8O_6$, AA, 99%) and polyvinylpyrrolidone ($(C_6H_9NO)_n$, PVP, average M.W. 58000) were purchased from J&K Scientific Ltd. Ethylene glycol ($C_2H_6O_2$, EG, reagent grade), potassium hydroxide (KOH, , reagent grade) and sulfuric acid (H_2SO_4, 95.0~98.0%) were purchased from Sinopharm Chemical Reagent Co. Ltd. Nafion solution (~5 wt% in a mixture of lower aliphatic alcohols and water) was purchased from Sigma-Aldrich. All the chemicals were used without further purification. The water (18 MΩ/cm) used in all experiments was prepared by passing through an ultra-pure purification system (Aqua Solutions).

Synthesis of pristine $IrTe_2$ hollow nanoshuttles ($IrTe_2$ HNSs). In a typical synthesis of $IrTe_2$ HNSs, $Ir(acac)_3$ (12.2 mg), K_2TeO_3 (12.7 mg), AA (36 mg) and PVP (100 mg) were mixed in 5 mL of EG, followed by the addition of DI water (5 mL) and ultrasonicated for approximately 0.5 h. The resulting homogeneous mixture was transferred into a 25 mL Teflon-lined stainless-steel autoclave. The sealed vessel was then heated at 200 ºC for 10 h before it was cooled down to room temperature. The products were collected via centrifugation and further purified by an ethanol-acetone mixture. The $IrTe_2$ HNSs were then supported on carbon (Vulcan XC-72R carbon black) with a target loading level of 20 wt% Ir (The loading amount is evaluated by the thermogravimetric analysis.). The obtained catalyst powder was annealed at 250 °C in H_2 (5 vol% in Ar) for 2 h for further use.

Characterization. Low-magnification transmission electron microscopy (TEM) was conducted on a HITACHI HT7700 transmission electron microscope at an accelerating voltage of 120 kV. High-resolution TEM (HRTEM), high-angle annular dark-field scanning TEM (HAADF-STEM) and HAADF-STEM energy-dispersive X-ray spectroscopy (HAADF-STEM-EDS) were conducted on an FEI Tecnai F20 transmission electron microscope at an acceleration voltage of 200 kV. Partial HAADF-STEM and HAADF-STEM-EDS were conducted on a JEOL GrandARM300F scanning transmission electron microscope with double Cs correctors at an acceleration voltage of 300 kV. Powder X-ray diffraction (PXRD) patterns were collected on a Shimadzu XRD-6000 X-ray diffractometer. Thermogravimetric analyses were performed on SII TG/DTA 6300 thermogravimetric analyzer at a heating rate of 10 ºC min^{-1} in air atmosphere. X-ray photoelectron spectroscopy (XPS) data were collected with a SSI S-Probe XPS Spectrometer. Operando X-ray absorption (XAS) measurements were conducted on the TPS-44A beamline of the Taiwan National Synchrotron Radiation Research Center (NSRRC).

Electrochemical measurements. A typical three-electrode cell was used to perform the electrochemical measurements. The working electrode was a glassy-carbon electrode (GCE) (diameter: 5 mm) from the Pine Instrument. A saturated calomel electrode (SCE) and a graphite rod were used as the reference and counter electrode, respectively. To prepare the working electrode, a certain amount of catalyst was mixed with 1 mL of ethanol and 10 μL of 5 wt% Nafion solution, and sonicated for 30 min to form a homogeneous catalyst ink. Then, 10 μL of catalyst ink was pipetted onto a pre-polished and cleaned GCE and dried under ambient condition. The loading amount of metal (Ir or Pt) on working electrode was controlled to be 4 μg for the hydrogen evolution reaction (HER) and 10 μg for the oxygen evolution reaction (OER), respectively. All electrochemical measurements were carried out in N_2-saturated electrolytes (e.g., 0.1 M KOH, 1.0 M KOH, 0.05 M H_2SO_4 and 0.5 M H_2SO_4) unless otherwise stated.

For the preparation of D-$IrTe_2$ HNSs for HER, the pristine $IrTe_2$ HNSs were "dealloyed" by potential cycling from 0.05 V to 1.1 V (vs RHE) for 50 cycles at 100 mV s^{-1} in 0.1 M KOH. The surface areas of Pt and Ir were determined from the hydrogen desorption charge ($Q_{H\text{-desorption}}$) with the charge densities of 210 μC cm^{-2}_{Pt} and 218 μC cm^{-2}_{Ir}, respectively[12]. For the preparation of DO-$IrTe_2$ HNSs for OER, the pristine $IrTe_2$ HNSs were "dealloyed" and oxidized by applying potential cycling from 0.05 V to 1.5 V for 50 cycles at 100 mV s^{-1} in 0.1 M KOH. For comparison, identical electrochemical treatment was performed for the commercial Ir/C catalyst (O-Ir/C). To estimate the number of accessible active sites, the catalysts were scanned between the potentials of 0.4 V and 1.4 V at 50 mV s^{-1} for 3 cycles in 0.05 M H_2SO_4. The number of electrochemical active Ir sites was estimated based on the anodic charge of oxidation peak with capacitance current subtraction[54].

To ensure that the observed oxidation current was from water oxidation, rotating ring-disk electrode (RRDE) measurement was performed. The disk current is fixed at a constant of 0.4 mA to generate O_2 molecules. A rotating Pt ring electrode held at a constant potential of 0.4 V vs. RHE to detect O_2 generated over the catalyst by electrochemical reduction (ORR). The O_2 collection efficiency as determined using the same configuration with IrO_2 catalyst is 0.17. All RRDE measurements were conducted at a rotation rate of 1600 rpm, and the electrolyte was pre-saturated with N_2 to eliminate dissolved oxygen.

TOF measurements. The TOF value was calculated from equation[55].

$$\text{TOF} = \frac{J * A}{N * F * n}$$

J is the recorded current density (A cm^{-2}), A is the geometric area of GCE (cm^2), N is the number of electrons required to form a molecule of product (N = 2 for HER, N = 4 for OER), F is the Faraday constant (C mol^{-1}), n is the number of active sites (mol) calculated via two methods.

For HER, the active sites could be identified to be the surface Ir or Pt atoms. Therefore, the number of active sites can be calculated from the hydrogen adsorption measurements. Assuming that each surface metal atom can adsorb one hydrogen atom, the number of active surface metal sites was calculated from the equation:

$$\text{n}_{\text{(active surface metal sites)}} = \frac{Q_{H\text{-}desorption} * N_A}{F}$$

where $Q_{H\text{-}desorption}$ is the hydrogen desorption charge, N_A is Avogadro's constant, F is the Faraday constant[12,56].

For OER, the active surface redox sites were determined by integrating the anodic oxidation peak of Ir without the capacitive current ($Q_{\text{Ir redox peak}}$)[54,57]. Since the oxidation only involves one electron transfer, the number of active surface redox sites was calculated from the equation:

$$\text{n}_{\text{(active surface redox sites)}} = \frac{Q_{\text{Ir redox peak}} * N_A}{F}$$

X-ray absorption spectroscopy (XAS) measurements. XAS data were collected at the TPS-44A beamline of the National Synchrotron Radiation Research Center (NSRRC, Hsinchu, Taiwan) using a Si (111) quick-scanning monochromator. Operando Ir-L_3 XANES and EXAFS spectra were measured in transmission mode at room temperature[58]. La_2CoIrO_6 was simultaneously measured for energy reference to rule out any energy drifts during the whole experiments[48]. The general set up is depicted in **Supplementary Fig. 24**. The TPS-44A beamline allows for the rapid collection of 240 Ir-L_3 *EXAFS* spectra within 2 minutes. All XAS data were firstly analyzed by using JAQ software and then processed according to standard procedures using the Demeter program package (Version 0.9.24)[59].

DFT Calculation. For studying the physicochemical trend as well as better understanding the electronic and energetic properties, we choose the simplified rotationally invariant DFT+U calculations[60] within CASTEP code[61] for calculating the electronic and energetic properties. The geometric optimization algorithm of Broyden-Fletcher-Goldfarb-Shannon (BFGS) has selected for ground state lattice relaxation and spurious strain release, especially for the interfacial relaxation. The cutoff energy of plane-wave basis sets for total energy and valence electronic states calculations has been set to 750 eV. The PBE exchange-correlation functional is selected for DFT+U calculations. To improve the convergence quality of transition metal compound system, the ensemble DFT (EDFT) by Marzari et al.[62] is used during electronic-minimization process.

The substrate $IrTe_2$ model was built based on the bulk $IrTe_2$ crystal with symmetry group *P-3M1*. The optimized hexagonal lattice parameters are a=b=3.930 Å, c=5.389 Å; $\alpha=\beta=90°$ and $\gamma=120°$. The de-alloyed Ir layer has been built based on the metallic Ir with 3.840 Å as the lattice parameter. The oxidized de-alloyed Ir layer has been built with two reduced IrO_2 surface layer with and without cracks. The IrO_2 surface layer has been modeled based on the bulk rutile IrO_2 lattice with optimized lattice parameters a=b=4.621 Å and c=3.026 Å. The Ir||IrTe2 interface system has been built with 6-layer-thick Ir-lattice and 6-bilayer-thick IrTe2 with approximated the range of 163-170 atom sized. The IrO_2||Ir||$IrTe_2$ interface system has been built with 6-layer-thick reduced IrO_2, 6-layer-thick Ir-lattice, and 6-bilayer-thick $IrTe_2$ with the range of 212-226 atom sized. Some portions of Ir and O sites have been manually deleted for simulating the IrO_2||Ir||$IrTe_2$ interface with cracks. We also provided the view of the local structural configuration, showing different H/O species as initial reactants, intermediates, and final products for illustrating the HER and OER occurred on the Ir||$IrTe_2$ and IrO_2||Ir||$IrTe_2$ interfaces respectively (**Supplementary Fig. 28**).

Considering the DFT computational cost, the Monkhost-Pack reciprocal space integration was performed using Gamma-center-off special k-points with mesh of 2×2×2 [63], which was guided by the initial convergence test. With these settings, the overall total energy for each step are converged to less than 5.0×10^{-7} eV per atom. The Hellmann-Feynman forces on the atom were converged to less than 0.001 eV/Å.

The Ir, Te, O, and H norm-conserving pseudopotentials are generated using the OPIUM code in the Kleinman-Bylander projector form[64], and the non-linear partial core correction[65] and a scalar relativistic averaging scheme[66] are used to treat the mixed valence Ir spin-orbital coupling effect. We chose the projector-based (5*d*, 6*s*, 6*p*), (5*s*, 5*p*), (2*s*, 2*p*), and (1*s*) states to reflect the valence states of Ir, Te, O, and H atoms, respectively. The RRKJ method is chosen for the optimization of the pseudopotentials[67].

References

1. Lewis, N. S. Research opportunities to advance solar energy utilization. *Science* **351**, aad1920 (2016).

2. Dunn, B., Kamath, H., Tarascon, J. M. Electrical energy storage for the grid: A battery of choices. *Science* **334**, 928-935 (2011).

3. Jiao, Y., Zheng, Y., Jaroniec, M., Qiao, S. Z. Design of electrocatalysts for oxygen- and hydrogen-involving energy conversion reactions. *Chem. Soc. Rev.* **44**, 2060-2086 (2015).

4. Li, M. *et al.* Ultrafine jagged platinum nanowires enable ultrahigh mass activity for the oxygen reduction reaction. *Science* **354**, 1414-1419 (2016).

5. Montoya, J. H., Seitz, L. C., Chakthranont, P., Vojvodic, A., Jaramillo, T. F., Norskov, J. K. Materials for solar fuels and chemicals. *Nat. Mater.* **16**, 70-81 (2017).

6. She, Z. W., Kibsgaard, J., Dickens, C. F., Chorkendorff, I., Nørskov, J. K., Jaramillo, T. F. Combining theory and experiment in electrocatalysis: Insights into materials design. *Science* **355**, eaad4998 (2017).

7. Han, N. *et al.* Ultrathin bismuth nanosheets from in situ topotactic transformation for selective electrocatalytic CO_2 reduction to formate. *Nat. Commun.* **9**, 1320 (2018).

8. Soloveichik, G. Electrochemical synthesis of ammonia as a potential alternative to the Haber–Bosch process. *Nat. Catal.* **2**, 377-380 (2019).

9. Huang, Z. F. *et al.* Chemical and structural origin of lattice oxygen oxidation in Co–Zn oxyhydroxide oxygen evolution electrocatalysts. *Nat. Energy* **4**, 329-338 (2019).

10. Yao, Z., Yan, J., Anthony, V., Qiao, S. Z. The hydrogen evolution reaction in alkaline solution: from theory, single crystal models, to practical electrocatalysts. *Angew. Chem. Int. Ed.* **57**, 7568-7579 (2018).

11. Zou, X., Zhang, Y. Noble metal-free hydrogen evolution catalysts for water splitting. *Chem. Soc. Rev.* **44**, 5148-5180 (2015).

12. Zheng, J., Sheng, W., Zhuang, Z., Xu, B., Yan, Y. Universal dependence of hydrogen oxidation and evolution reaction activity of platinum-group metals on pH and hydrogen binding energy. *Sci. Adv.* **2**, e1501602 (2016).

13. McCrory, C. C. L., Jung, S., Ferrer, I. M., Chatman, S. M., Peters, J. C., Jaramillo, T. F. Benchmarking hydrogen evolving reaction and oxygen evolving reaction electrocatalysts for solar water splitting devices. *J. Am. Chem. Soc.* **137**, 4347-4357 (2015).

14. Feng, J. *et al.* Iridium-Based Multimetallic Porous Hollow Nanocrystals for Efficient Overall-Water-Splitting Catalysis. *Adv Mater*, **29**, 1703798 (2017).

15. Stamenkovic, V. R. *et al.* Improved oxygen reduction activity on Pt_3Ni (111) via increased surface site availability. *Science* **315**, 493-497 (2007).

16. Suntivich, J., May, K. J., Gasteiger, H. A., Goodenough, J. B., Shao-Horn Y. A perovskite oxide optimized for oxygen evolution catalysis from molecular orbital principles. *Science* **334**, 1383-1385 (2011).

17. Zhang, J., Yang, H., Fang, J., Zou, S. Synthesis and oxygen reduction activity of shape-controlled Pt_3Ni nanopolyhedra. *Nano Lett.* **10**, 638-644 (2010).

18. Choi, S. I. *et al.* Synthesis and characterization of 9 nm Pt–Ni octahedra with a record high activity of 3.3 A/mg_{Pt} for the oxygen reduction reaction. *Nano Lett.* **13**, 3420-3425 (2013).

19. Beermann, V. *et al.* Rh-doped Pt–Ni octahedral nanoparticles: Understanding the correlation between elemental distribution, oxygen reduction reaction, and shape stability. *Nano Lett.* **16**, 1719-1725 (2016).

20. Carpenter, M.K., Moylan, T. E., Kukreja, R. S., Atwan, M. H., Tessema, M. M. Solvothermal synthesis of platinum alloy nanoparticles for oxygen reduction electrocatalysis. *J. Am. Chem. Soc.* **134**, 8535-8542 (2012).

21. Cui, C., Gan, L., Heggen, M., Rudi, S., Strasser, P. Compositional segregation in shaped Pt alloy nanoparticles and their structural behaviour during electrocatalysis. *Nat. Mater.* **12**, 765-771 (2013).

22. Chattot, R. *et al.* Surface distortion as a unifying concept and descriptor in oxygen reduction reaction electrocatalysis. *Nat. Mater.* **17**, 827-833 (2018).

23. Chen, Y. *et al.* Exceptionally active iridium evolved from a pseudo-cubic perovskite for oxygen evolution in acid. *Nat. Commun.* **10**, 572 (2019).

24. Fabbri, E. *et al.* Dynamic surface self-reconstruction is the key of highly active perovskite nano-electrocatalysts for water splitting. *Nat. Mater.* **16**, 925-931 (2017).

25. Seitz, L. C. *et al.* A highly active and stable $IrO_x/SrIrO_3$ catalyst for the oxygen evolution reaction. *Science* **353**, 1011-1014 (2016).

26. Li, J. *et al.* Surface evolution of a Pt–Pd–Au electrocatalyst for stable oxygen reduction. *Nat. Energy* **2**, 17111 (2017).

27. Nong, H. N. *et al.* A unique oxygen ligand environment facilitates water oxidation in hole-doped $IrNiO_x$ core–shell electrocatalysts. *Nat. Catal.* **1**, 841-851 (2018).

28. Yan, D., Li, Y., Huo, J., Chen, R., Dai, L., Wang, S. Defect chemistry of nonprecious-metal electrocatalysts for oxygen reactions. *Adv. Mater.* **29**, 1606459 (2017).

29. Jia, Y. *et al.* Defect graphene as a trifunctional catalyst for electrochemical reactions. *Adv. Mater.* **28**, 9532-9538 (2016).

30. Lv, C. *et al.* Defect engineering metal-free polymeric carbon nitride electrocatalyst for effective nitrogen fixation under ambient conditions. *Angew. Chem. Int. Ed.* **57**, 10246-10250 (2018).

31. Li, Y, H*, et al.* Local atomic structure modulations activate metal oxide as electrocatalyst for hydrogen evolution in acidic water. *Nat. Commun.* **6**, 8064 (2015).

32. Ling, T. *et al.* Engineering surface atomic structure of single-crystal cobalt (II) oxide nanorods for superior electrocatalysis. *Nat. Commun.* **7**, 12876 (2016).

33. Xu, L. *et al.* Plasma-engraved Co_3O_4 nanosheets with oxygen vacancies and high surface area for the oxygen evolution reaction. *Angew. Chem. Int. Ed.* **55**, 5277-5281 (2016).

34. Gao, S. *et al.* Atomic layer confined vacancies for atomic-level insights into carbon dioxide electroreduction. *Nat. Commun.* **8**, 14503 (2017).

35. Li, B. Q., Xia, Z. J., Zhang, B., Tang, C., Wang, H. F., Zhang, Q. Regulating p-block metals in perovskite nanodots for efficient electrocatalytic water oxidation. *Nat. Commun.* **8**, 934 (2017).

36. Wu, J., Qi, L., You, H., Gross, A., Li, J., Yang, H. Icosahedral platinum alloy nanocrystals with enhanced electrocatalytic activities. *J. Am. Chem. Soc.* **134**, 11880-11883 (2012).

37. Yang, H., Finefrock, S. W., Albarracin Caballero, J. D., Wu, Y. Environmentally benign synthesis of ultrathin metal telluride nanowires. *J. Am. Chem. Soc.* **136**, 10242-10245 (2014).

38. Pourbaix, M. Atlas of Electrochemical Equilibria in Aqueous Solutions (US National Association of Corrosion Engineers, 1974).

39. Suen, N. T., Hung, S. F., Quan, Q., Zhang, N., Xu, Y. J., Chen, H. M. Electrocatalysis for the oxygen evolution reaction: recent development and future perspectives. *Chem. Soc. Rev.* **46**, 337-365 (2017).

40. Luo, J. *et al.* Water photolysis at 12.3% efficiency via perovskite photovoltaics and Earth-abundant catalysts. *Science* **345**, 1593-1596 (2014).

41. Ping, J. *et al.* Self-assembly of single-layer CoAl-layered double hydroxide nanosheets on 3D graphene network used as highly efficient electrocatalyst for oxygen evolution reaction. *Adv. Mater*. **28**, 7640-7645 (2016).

42. McCrory, C. C. L., Jung, S., Peters, J. C., Jaramillo, T. F. Benchmarking heterogeneous electrocatalysts for the oxygen evolution reaction. *J. Am. Chem. Soc.* **135**, 16977-16987 (2013).

43. Yang, L. *et al.* Efficient oxygen evolution electrocatalysis in acid by a perovskite with face-sharing IrO_6 octahedral dimers. *Nat. Commun.* **9**, 5236 (2018).

44. Kumari, S., Ajayi, B. P., Kumar, B., Jasinski, J. B., Sunkara, M. K., Spurgeon, J. M. A low-noble-metal $W_{1-x}Ir_xO_{3-\delta}$ water oxidation electrocatalyst for acidic media via rapid plasma synthesis. *Energy Environ. Sci.* **10**, 2432-2440 (2017).

45. Shan, J., Ling, T., Davey, K., Zheng, Y., Qiao, S. Z. Transition-metal-doped RuIr bifunctional nanocrystals for overall water splitting in acidic environments. *Adv. Mater.* **31**, 1900510 (2019).

46. Park, J., Sa, Y. J., Baik, H., Kwon, T., Joo, S. H., Lee, K. Iridium-based multimetallic nanoframe@nanoframe structure: An efficient and robust electrocatalyst toward oxygen evolution reaction. *ACS Nano* **11**, 5500-5509 (2017).

47. Jiang, Q., Xu, L., Chen, N., Zhang, H., Dai, L., Wang, S. Facile synthesis of black phosphorus: An efficient electrocatalyst for the oxygen evolving reaction. *Angew. Chem. Int. Ed*. **55**, 13849-13853 (2016).

48. Agrestini, S. *et al.* Nature of the magnetism of iridium in the double perovskite Sr_2CoIrO_6. *Phys. Rev. B* **100**, 014443 (2019).

49. Choy, J. H., Kim, D. K., Hwang, S. H., Demazeau, G., Jung, D. Y. XANES and EXAFS studies on the Ir-O bond covalency in ionic iridium perovskites. *J. Am. Chem. Soc.* **117**, 8557-8566 (1995).

50. Abbott, D. F. *et al.* Iridium oxide for the oxygen evolution reaction: Correlation between particle size, morphology, and the surface hydroxo layer from operando XAS. *Chem. Mater.* **28**, 6591-6604 (2016).

51. Ni, B., Wang, X. Face the edges: Catalytic active sites of nanomaterials. *Adv. Sci.* **2**, 1500085 (2015).

52. Ping, Y., Nielsen, R. J., Goddard, W. A. The reaction mechanism with free energy barriers at constant potentials for the oxygen evolution reaction at the IrO_2 (110) surface. *J. Am. Chem. Soc.* **139**, 149-155 (2017).

53. Ling, T. *et al.* Activating cobalt(II) oxide nanorods for efficient electrocatalysis by strain engineering. *Nat. Commun.* **8**, 1509 (2017).

54. Lettenmeier, P. *et al.* Nanosized IrO_x–Ir catalyst with relevant activity for anodes of proton exchange membrane electrolysis produced by a cost-effective procedure. *Angew. Chem. Int. Ed.* **55**, 742-746 (2016).

55. Zhang, B. *et al.* Homogeneously dispersed, multimetal oxygen-evolving catalysts. *Science* **352**, 333-337 (2016).

56. Woods, R. Hydrogen adsorption on platinum, iridium and rhodium electrodes at reduced temperatures and the determination of real surface area. *J. Electroanal. Chem. Interfacial Electrochem.* **49**, 217-226 (1974).

57. Nong, H. N., Gan, L., Willinger, E., Teschner, D., Strasser, P. IrO_x core-shell nanocatalysts for cost- and energy-efficient electrochemical water splitting. *Chem. Sci.* **5**, 2955-2963 (2014).

58. Müller, O., Lützenkirchen-Hecht, D., Frahm, R. Quick scanning monochromator for millisecond in situ and in operando X-ray absorption spectroscopy. *Rev. Sci. Instrum.* **86**, 093905 (2015).

59. Ravel, B., Newville, M. ATHENA, ARTEMIS, HEPHAESTUS: Data analysis for X-ray absorption spectroscopy using IFEFFIT. *J. Synchrotron Radiat.* **12**, 537-541 (2005).

60. Anisimov, V. I., Aryasetiawan, F., Lichtenstein, A. I. First-principles calculations of the electronic structure and spectra of strongly correlated systems: the LDA + Umethod. *J. Phys. Condens. Matter* **9**, 767-808 (1997).

61. Clark, S. J., Segall, M. D., Pickard, C. J., Hasnip, P. J., Probert, M. I. J., Refson, K., Payne, M. C. First principles methods using CASTEP. *Zeitschrift für Kristallographie - Crystalline Materials* **220**, 567-570 (2005).

62. Marzari, N., Vanderbilt, D., Payne, M. C. Ensemble density-functional theory for ab initio molecular dynamics of metals and finite-temperature insulators. *Phys. Rev. Lett.* **79**, 1337-1340 (1997).

63. Probert, M. I. J., Payne, M. C. Improving the convergence of defect calculations in supercells: An *ab initio* study of the neutral silicon vacancy. *Phys. Rev. B* **67**, 075204 (2003).

64. Kleinman, L., Bylander, D. M. Efficacious form for model pseudopotentials. *Phys. Rev. Lett.* **48**, 1425-1428 (1982).

65. Louie, S. G., Froyen, S., Cohen, M. L. Nonlinear ionic pseudopotentials in spin-density-functional calculations. *Phys. Rev. B* **26**, 1738-1742 (1982).

66. Grinberg, I., Ramer, N. J., Rappe, A. M. Transferable relativistic Dirac-Slater pseudopotentials. *Phys. Rev. B* **62**, 2311-2314 (2000).

67. Rappe, A. M., Rabe, K. M., Kaxiras, E., Joannopoulos, J. D. Optimized pseudopotentials. *Phys. Rev. B* **41**, 1227-1230 (1990).

Acknowledgment

This work was financially supported by the Ministry of Science and Technology of China (2016YFA0204100, 2017YFA0208200), the National Natural Science Foundation of China (21571135), Young Thousand Talented Program, Jiangsu Province Natural Science Fund for Distinguished Young Scholars (BK20170003), the project of scientific and technologic infrastructure of Suzhou (SZS201708), the Priority Academic Program Development of Jiangsu Higher Education Institutions (PAPD), and the start-up supports from Soochow University. The research in Dresden was partially supported by the DFG through SFB 1143. We acknowledge the support from the Max Planck-POSTECH-Hsinchu Center for Complex Phase Materials.

Author contributions

X.H. conceived and supervised the research. X.H., Y.P. and L.B. designed the experiments. X.H., Y.P. and L.B. performed most of the experiments and data analysis. X.H., Y.P. and L.B. participated in various aspects of the experiments and discussions. Y.M. and T.S. performed electron microscopy experiments and structure analysis. B.H performed the DFT simulations. X.H., Y.P., L.L and L.B. wrote the paper. X.H., Y.P., Z.H. and C.P. performed the XAS experiments and data analysis. All authors discussed the results and commented on the manuscript.

Additional information

Supplementary Information is linked to the online version of this paper at http://www.nature.com/.

Competing financial interests

The authors declare no competing financial interests.

Reprint and permissions information is available at http://www.nature.com/.

Correspondence and requests for materials should be addressed to B.H. (bhuang@polyu.edu.hk) and X.H. (hxq006@suda.edu.cn).

Figures

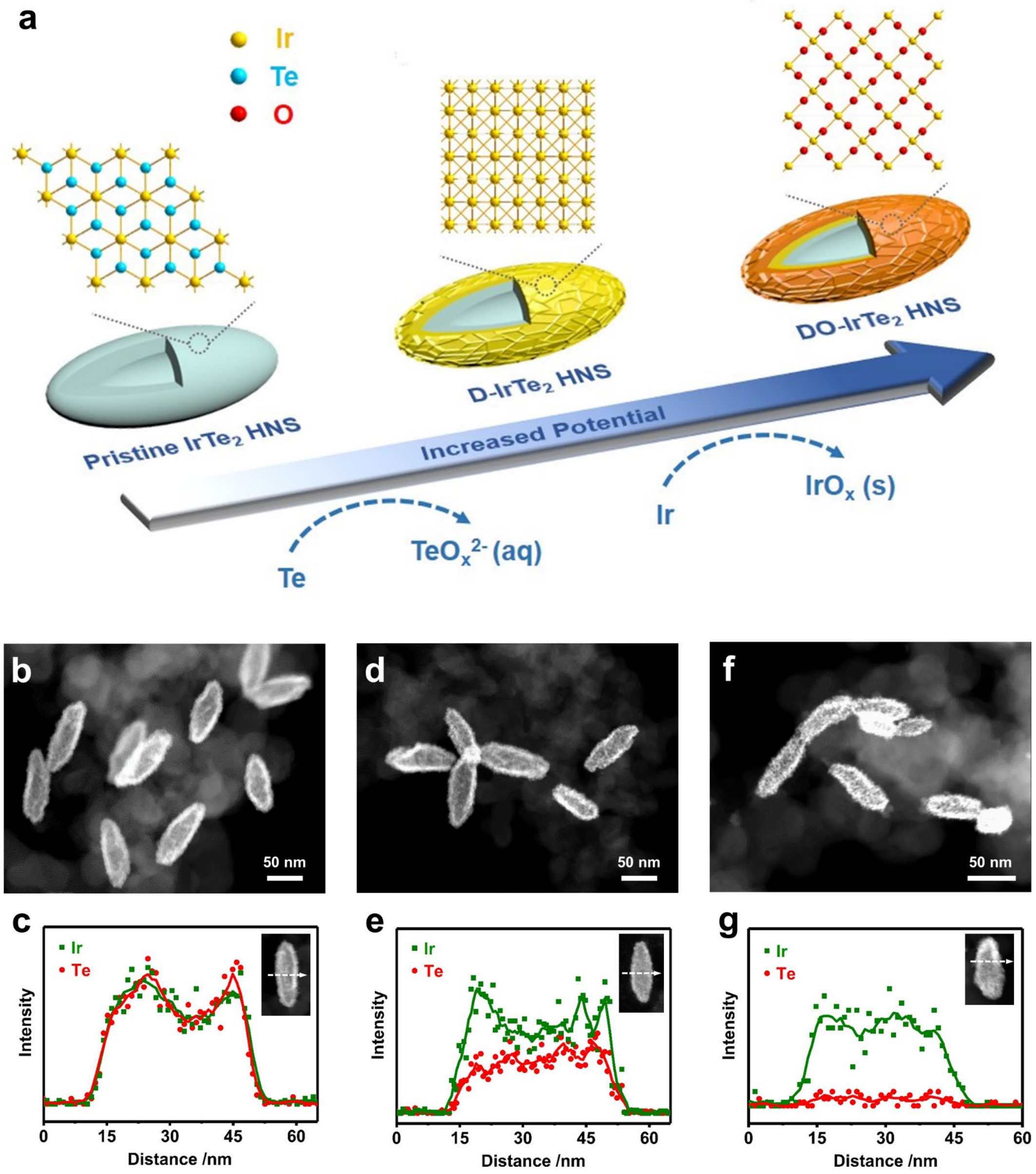

Figure 1. | Fabrication of D-IrTe$_2$ and DO-IrTe$_2$ HNSs from pristine IrTe$_2$ HNSs. (**a**) Schematic illustration of the precise electrochemical evolution. Pristine IrTe$_2$ HNSs are dealloyed at mild potential to form D-IrTe$_2$ HNSs with metallic surface, or dealloyed at higher potential to form DO-IrTe$_2$ HNSs with oxidized surface. (**b**, **d**, **f**) HAADF-STEM images and (**c**, **e**, **g**) EDS line scan analysis (Ir in green and Te in red) of (**b, c**) pristine IrTe$_2$ HNSs, (**d, e**) D-IrTe$_2$ HNSs and (**f, g**) DO-IrTe$_2$ HNSs.

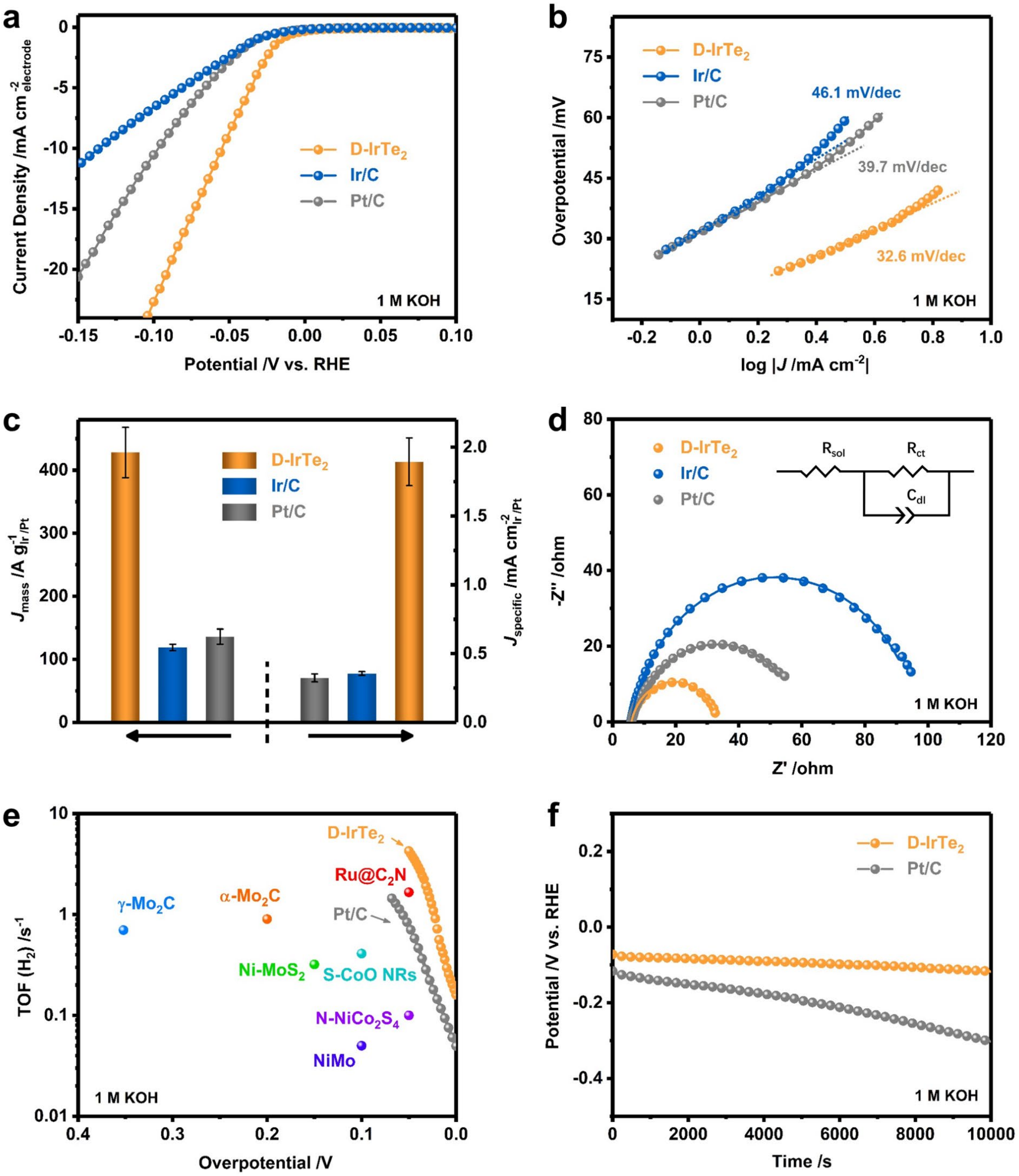

Figure 2. | HER performance of D-IrTe$_2$ HNSs. (**a**) Polarization curves, (**b**) Tafel plots, and (**c**) mass activity (left) and specific activity (right) of D-IrTe$_2$ HNSs, Ir/C and Pt/C in 1.0 M KOH solution. (**d**) Electrochemical impedance spectra of D-IrTe$_2$ HNSs, Ir/C and Pt/C. (**e**) Comparison of the TOF of D-IrTe$_2$ HNSs with other reported catalysts. (**f**) Durability test of D-IrTe$_2$ HNSs and Pt/C. The polarization curves were recorded at a constant current density of 10 mA cm^{-2} in 1.0 M KOH.

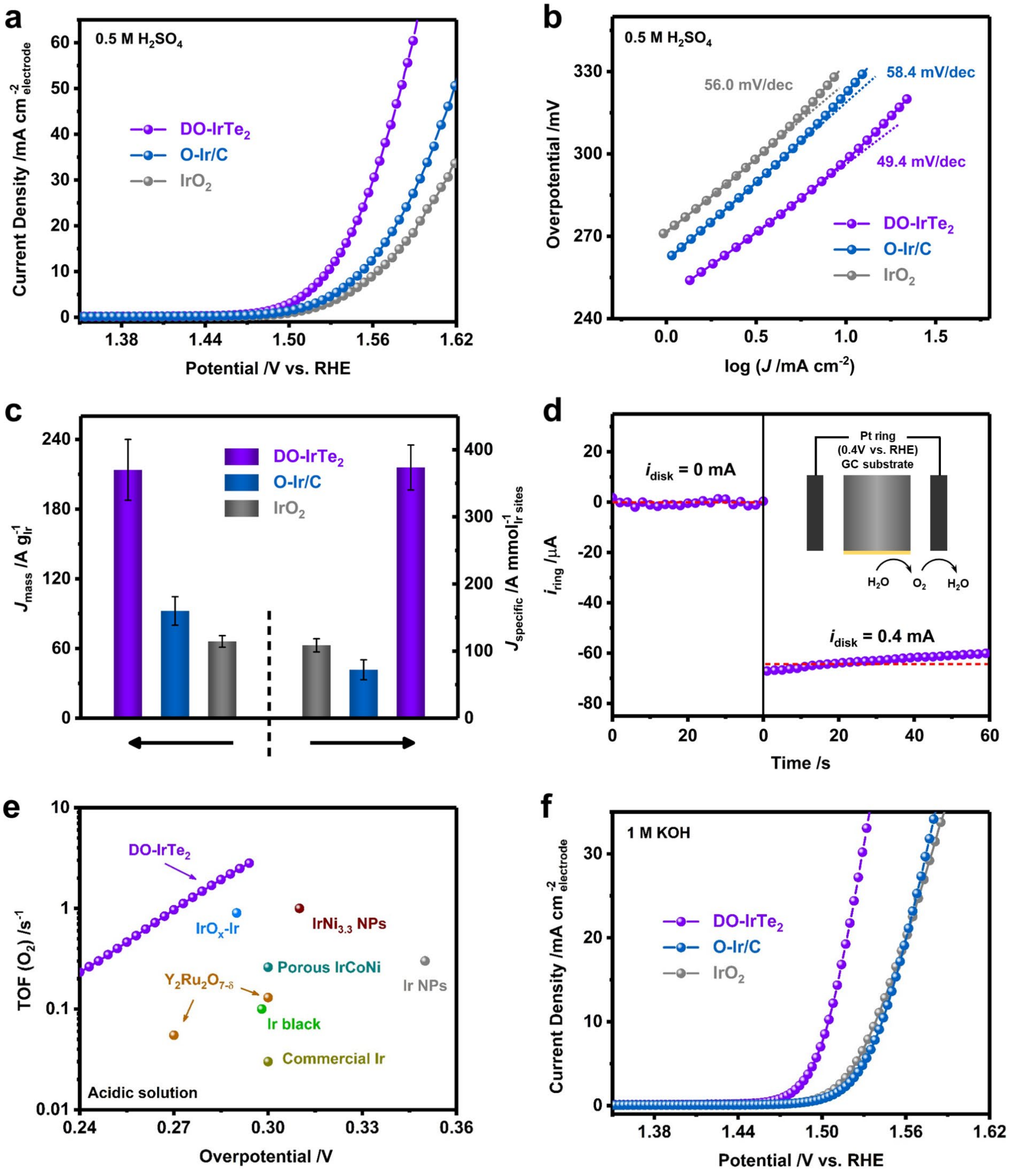

Figure 3. | OER performance of DO-IrTe$_2$ HNSs. (**a**) Polarization curves and (**b**) Tafel plots of DO-IrTe$_2$ HNSs, O-Ir/C and IrO$_2$ in 0.5 M H_2SO_4 solution. (**c**) Mass activity (left) and specific activity (right) of DO-IrTe$_2$ HNSs, O-Ir/C and IrO$_2$. (**d**) Ring current of DO-IrTe$_2$ HNSs on an RRDE (1600 rpm) with a ring potential of 0.4 V (schematic shown as an inset). (**e**) Comparison of the TOF of DO-IrTe$_2$ HNSs with other reported catalysts. (**f**) Polarization curves of DO-IrTe$_2$ HNSs, O-Ir/C and IrO$_2$ in 1.0 M KOH.

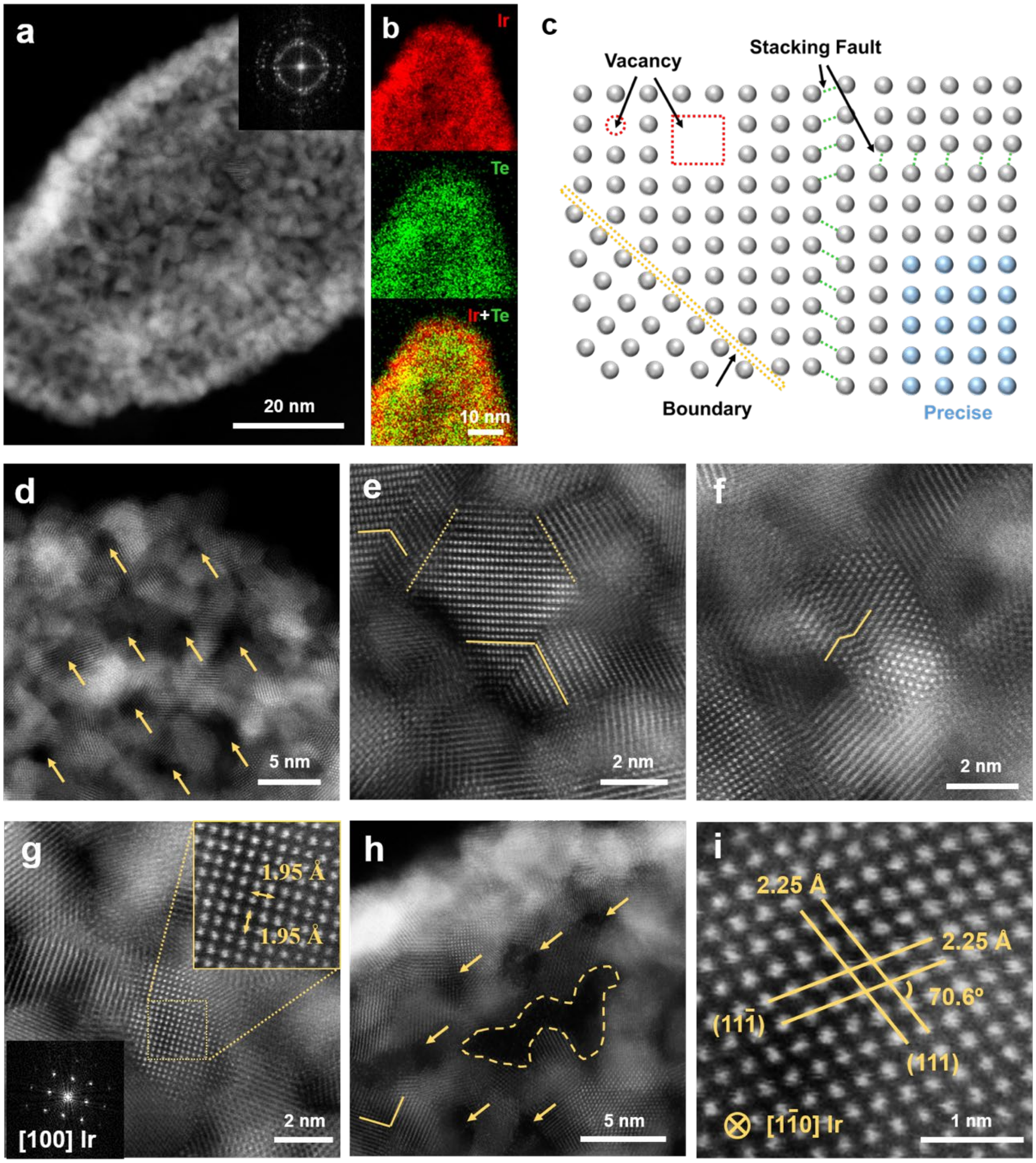

Figure 4. | Structural analysis of the local disorder configuration in D-IrTe$_2$ and DO-IrTe$_2$ HNSs. (**a**) HAADF-STEM image with inset showing its associated FFT pattern, (**b**) high-resolution elemental mappings of D-IrTe$_2$ HNS. (**c**) Schematic of local disorder atomic configuration, which contains the disordered regions with various defects (vacancies, boundaries, and stacking faults) and ordered region with precise atomic arrangement. Atomic-resolution HAADF-HRSTEM images of (**d-g**) D-IrTe$_2$ and (**h-i**) DO-IrTe$_2$ HNSs. The yellow arrows and dashed/solid lines in **d-f** and **h** highlight the various defects.

The dotted box in **g** and **i** highlights the ordered regions.

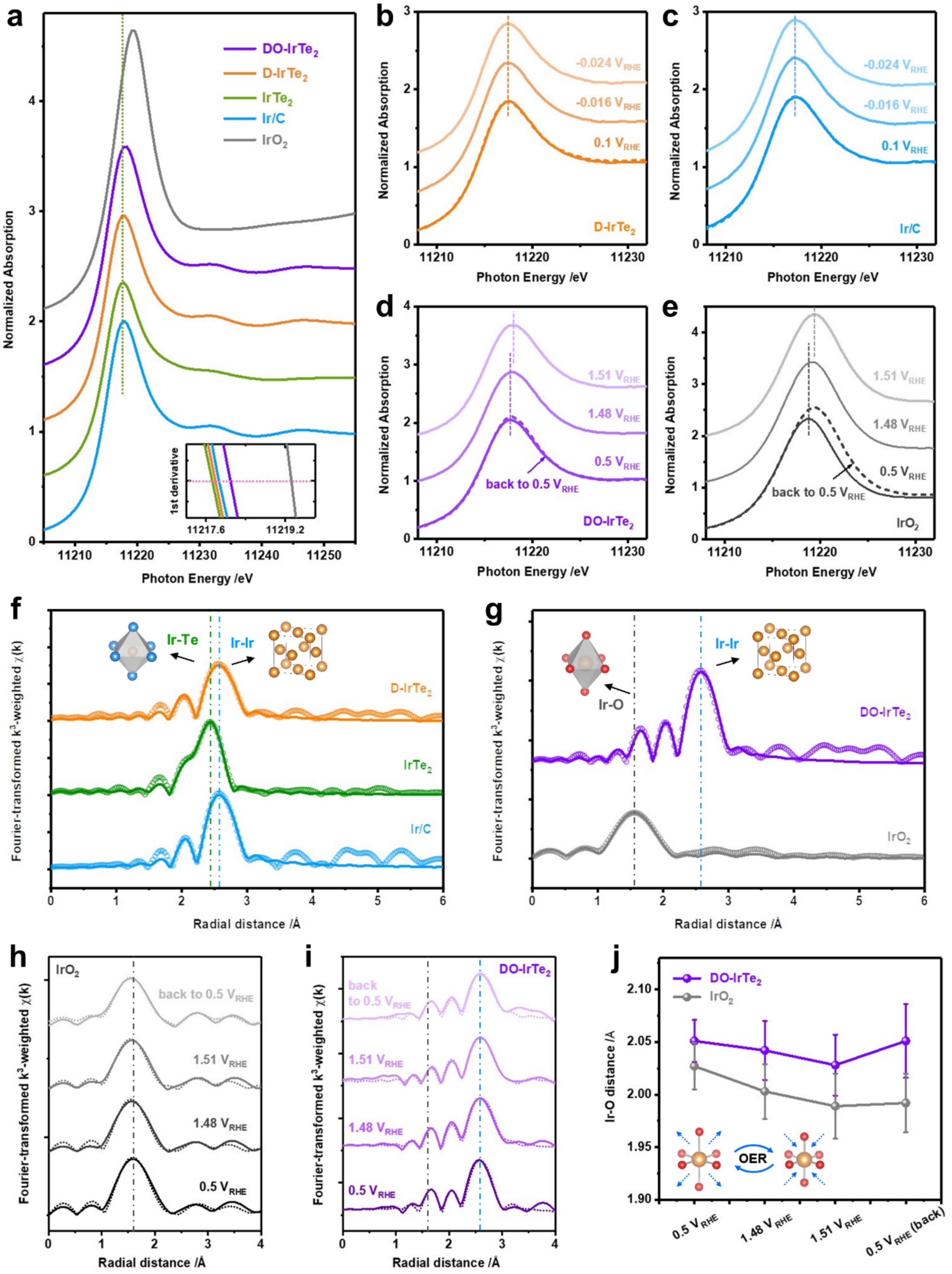

Figure 5. | Electronic and local structure of Ir centres in DO-IrTe$_2$ HNSs and D-IrTe$_2$ HNSs. (**a**) Normalized Ir L$_3$-edge XANES spectra of DO-IrTe$_2$ HNSs and D-IrTe$_2$ HNSs. Pristine IrTe$_2$ HNSs,

commercial Ir/C and IrO_2 are included as references. Normalized XANES spectra for (**b**) D-$IrTe_2$ HNSs, (**c**) Ir/C, (**d**) DO-$IrTe_2$ HNSs and (**e**) IrO_2 recorded at different potentials. The dotted lines in figures **b-e** present the spectra obtained when applied potential switched back to the initial values. (**f-g**) k^3-weighted Fourier transforms of EXAFS spectra of DO-$IrTe_2$ HNSs and D-$IrTe_2$ HNSs. Bulk $IrTe_2$, Ir/C and rutile-type IrO_2 are included as references. k^3-weighted Fourier transforms of EXAFS spectra for (**h**) IrO_2 and (**i**) DO-$IrTe_2$ HNSs recorded at different potentials. Vertical dashed lines indicate Ir-O (grey) and Ir-Ir (blue) radial distances for the IrO_2 and Ir/C, respectively. (**j**) The Ir-O distance in DO-$IrTe_2$ HNSs and IrO_2 determined from EXAFS analsis as a function of the allied potentials.

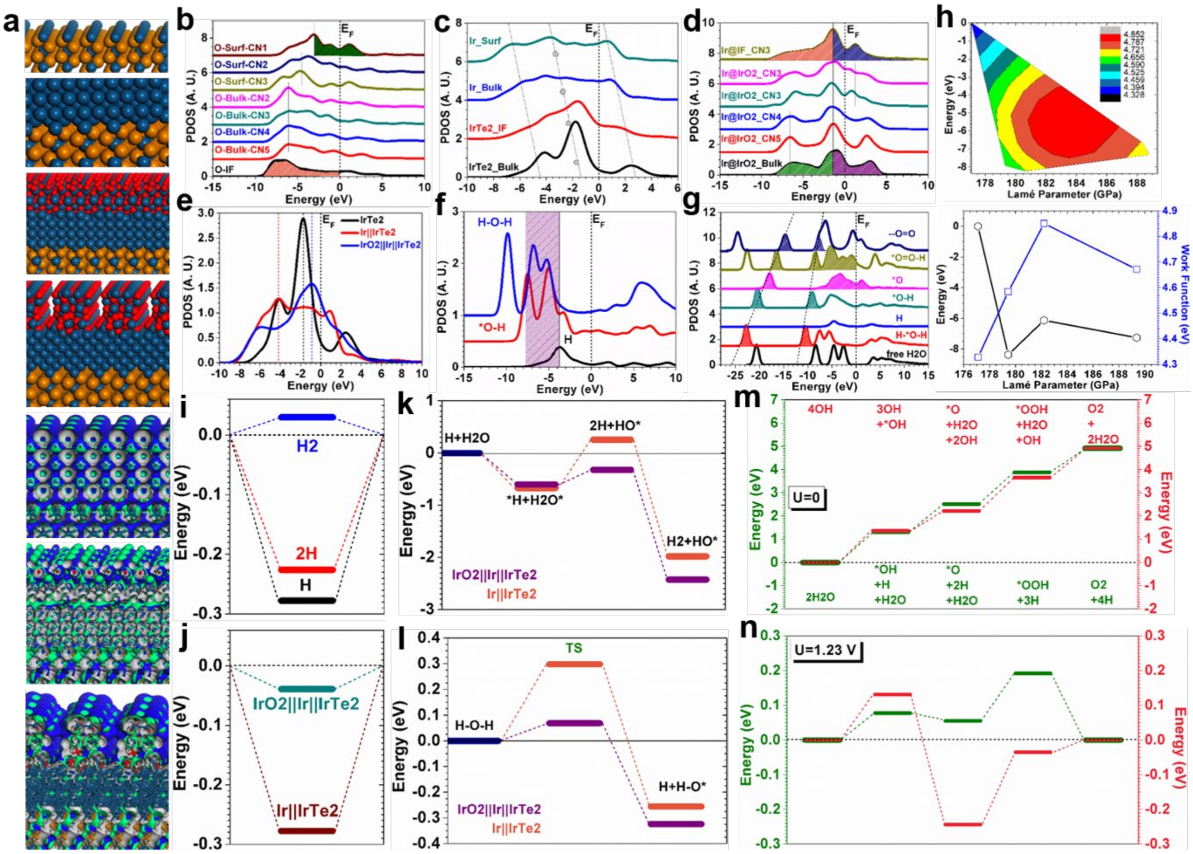

Figure 6. | Theoretically interpreted electronic and energetic activities for HER and OER. (a) Structural configurations of $IrTe_2$, Ir||$IrTe_2$, IrO_2||Ir||$IrTe_2$ and IrO_2||Ir||$IrTe_2$ with cracks. The real spatial

3D orbital contour plots of Ir||$IrTe_2$, IrO_2||Ir||$IrTe_2$ and IrO_2||Ir||$IrTe_2$ with cracks have been also provided. (b) The lay-out p-orbitals of lattice O-sites varying from the interface (IrO_2||Ir) region, bulk IrO_2, and IrO_2 surface region (CN=coordination number). (c) PDOSs of Ir-5*d* bands for different Ir-sites from $IrTe_2$ bulk, interface (Ir||$IrTe_2$), Ir-Bulk, and Ir-surface. (d) PDOSs of Ir-5*d* bands for different Ir-sites from IrO_2 bulk, surface region with different CNs, and interface (IF) region. (e) PDOSs of summed Ir-5*d* orbitals among $IrTe_2$, Ir, and IrO_2 systems. (f) PDOSs of different intermediate species of alkaline HER (H2O, *OH, and H). (g) PDOSs of intermediate O-species of four-electron based acidic OER. (h) Mapping and plots indicating the correlation with stabilities, mechanical modulus and work functions for different IF systems. (i) Adsorption energy comparison of H, 2H and H2. (j) The H-adsorption energy comparison between IrO_2||Ir||$IrTe_2$ and Ir||$IrTe_2$. (k) The pathway of alkaline HER occurred between IrO_2||Ir||$IrTe_2$ and Ir||$IrTe_2$ systems. (l) The H_2O splitting energetic levels with transition state (TS) representing the splitting barrier. (m) The pathways of both four-electron based acidic and alkaline OER at U=0 V. (n) The OER pathways are summarized at U=1.23 V.